A&A 521, L32 (2010)
DOI: 10.1051/0004-6361/201015103

Herschel/HIFI: first science highlights

Astronomy & Astrophysics
Special feature

Letter to the Editor

Water abundances in high-mass protostellar envelopes: *Herschel* observations with HIFI⋆,⋆⋆

M. G. Marseille[10], F. F. S. van der Tak[10,11], F. Herpin[6], F. Wyrowski[30], L. Chavarría[6], B. Pietropaoli[6], A. Baudry[6], S. Bontemps[6], J. Cernicharo[16], T. Jacq[5], W. Frieswijk[10], R. Shipman[10], E. F. van Dishoeck[1,2], R. Bachiller[12], M. Benedettini[13], A. O. Benz[3], E. Bergin[14], P. Bjerkeli[9], G. A. Blake[15], J. Braine[6], S. Bruderer[3], P. Caselli[4,5], E. Caux[36,37], C. Codella[5], F. Daniel[16], P. Dieleman[10], A. M. di Giorgio[13], C. Dominik[17,18], S. D. Doty[19], P. Encrenaz[20], M. Fich[21], A. Fuente[22], T. Gaier[31], T. Giannini[23], J. R. Goicoechea[16], Th. de Graauw[10], F. Helmich[10], G. J. Herczeg[2], M. R. Hogerheijde[1], B. Jackson[10], H. Javadi[31], W. Jellema[10], D. Johnstone[7,8], J. K. Jørgensen[24], D. Kester[10], L. E. Kristensen[1], B. Larsson[25], W. Laauwen[10], D. Lis[26], R. Liseau[9], W. Luinge[10], C. McCoey[21,27], A. Megej[35], G. Melnick[28], D. Neufeld[29], B. Nisini[23], M. Olberg[9], B. Parise[30], J. C. Pearson[31], R. Plume[32], C. Risacher[10], P. Roelfsema[10], J. Santiago-García[33], P. Saraceno[13], P. Siegel[31], J. Stutzki[34], M. Tafalla[12], T. A. van Kempen[28], R. Visser[1], S. F. Wampfler[3], and U. A. Yıldız[1]

(Affiliations are available on page 5 of the online edition)

Received 31 May 2010 / Accepted 15 July 2010

ABSTRACT

Aims. We derive the dense core structure and the water abundance in four massive star-forming regions in the hope of understanding the earliest stages of massive star formation.

Methods. We present *Herschel*/HIFI observations of the para-H_2O $1_{11}-0_{00}$ and $2_{02}-1_{11}$ and the para-$H_2^{18}O$ $1_{11}-0_{00}$ transitions. The envelope contribution to the line profiles is separated from contributions by outflows and foreground clouds. The envelope contribution is modeled with Monte-Carlo radiative transfer codes for dust and molecular lines (MC3D and RATRAN), and the water abundance and the turbulent velocity width as free parameters.

Results. While the outflows are mostly seen in emission in high-J lines, envelopes are seen in absorption in ground-state lines, which are almost saturated. The derived water abundances range from 5×10^{-10} to 4×10^{-8} in the outer envelopes. We detect cold clouds surrounding the protostar envelope, thanks to the very high quality of the *Herschel*/HIFI data and the unique ability of water to probe them. Several foreground clouds are also detected along the line of sight.

Conclusions. The low H_2O abundances in massive dense cores are in accordance with the expectation that high densities and low temperatures lead to freeze-out of water on dust grains. The spread in abundance values is not clearly linked to physical properties of the sources.

Key words. dust, extinction – ISM: molecules – ISM: abundances

1. Introduction

Massive stars ($\gtrsim 10\ M_\odot$) play a major role in the interstellar energy budget and the shaping of the Galactic environment (Zinnecker & Yorke 2007). However, the formation of such high-mass stars is not well understood for several reasons: they are rare, have a short evolution time scale, are born deeply embedded, and are far from the solar system.

The main-sequence lifetime of massive stars is preceded by an embedded phase that subdivides into several classes of objects: massive pre-stellar cores (mPSC), which are local temperature minima and density maxima within dark clouds (Sridharan et al. 2005); high-mass protostellar objects (HMPO), where a central protostar is surrounded by a massive envelope with a centrally peaked temperature and density distribution (van der Tak et al. 2000); hot molecular cores (HMC), which have higher masses of warm gas and dust and high abundances of complex organic molecules, which have evaporated off dust grains and/or formed by warm gas-phase chemistry (Motte et al. 2003); and ultracompact H I regions (UCHII), which show large pockets of ionized gas confined to the star (Churchwell et al. 1990). A key question is to what extent these phases represent differences in luminosity and/or age, and if all high-mass stars pass through all these phases.

The water molecule is thought to be a sensitive tracer of physical conditions in star-forming regions, which acts as a natural filter for warm gas because of its large abundance variations between hot and cold regions (van der Tak et al. 2006). Moreover, because the dust continuum is strong at the higher frequencies, water lines connecting with the lowest energy levels can be seen in absorption, thus providing an alternative method probing different depths in the protostellar environment (Poelman & van der Tak 2007). Measurements of the abundance of water are therefore a step toward understanding the energy budget of star-forming regions, hence of the star formation process itself.

This paper presents water observations performed with the Heterodyne Instrument for the Far Infrared (HIFI; de Graauw & et al. 2010) onboard ESA's *Herschel* Space Observatory (Pilbratt & et al. 2010). We use the p-H_2O ground-state line and two lines that constrain the excitation and optical depth (Table 1), all three

⋆ *Herschel* is an ESA space observatory with science instruments provided by European-led Principal Investigator consortia and with important participation of NASA.

⋆⋆ Appendix (pages 6 to 7) is only available in electronic form at http://www.aanda.org

Table 1. List of lines.

Molecule	Transition	ν (GHz)	E_{up} (K)	$n_{crit}{}^{a}$ (cm^{-3})	σ_{rms} (mK)
H_2O	$1_{11}-0_{00}$	1113.343	53.4	1.7×10^8	40
H_2O	$2_{02}-1_{11}$	987.927	100.8	2.1×10^8	50
$H_2^{18}O$	$1_{11}-0_{00}$	1101.698	53.4	1.7×10^8	40

Notes. [(a)] Values at 20 K from collision rates of Grosjean et al. (2003).

Table 2. List of sources.

Name	RA J2000	Dec. J2000	L (10^4 $L_\odot$)	d^a (kpc)	V_{LSR} (km s^{-1})
G31.41+0.31	$18^h47^m34.3^s$	$-01°12'46.0''$	15	7.9	+98.8
G29.96-0.02	$18^h46^m03.8^s$	$-02°39'22.0''$	20	7.4	+98.7
W33A	$18^h14^m39.1^s$	$-17°52'07.0''$	8.5	4.0	+37.5
W43-MM1	$18^h47^m47.0^s$	$-01°54'28.0''$	2.2	5.5	+98.8

Notes. [(a)] Values from Hatchell & van der Tak (2003), except W43-MM1 (Motte et al. 2003) and W33A (van der Tak et al. 2000).

lying at similar frequencies and observed at similar resolution. The sources are four massive star-forming regions (Table 2): the HMCs G31.41+0.31 and G29.96−0.02 and the HMPOs W33A and W43-MM1. We compare our results with those for two other regions: the UCHII region DR21 (van der Tak et al. 2010) and the HMPO W3 IRS5 (Chavarría et al. 2010).

However, the aim is to discover trends in the water line emission for future extended studies, identifying links in the water abundance between the various evolutionary stages of high-mass star formation and using water to probe the gas dynamics around protostars. Given the small number of sources and lines observed, it is premature to look for general trends. The large amount of upcoming *Herschel*/HIFI data will help with this question.

2. Observations

The four regions have been observed with HIFI on 3, 4, and 6 March 2010 (see Table 2). Spectra were taken in double sideband mode using receivers 4a (p-H_2O at 988 GHz) and 4b (p-H_2O and p-$H_2^{18}O$ at 1113 GHz and 1102 GHz) with ν_{LO} = 980 GHz and 1108 GHz, respectively. The observations are part of the priority science program (PSP) of the guaranteed-time key program *Water In Star-forming regions with Herschel* (WISH; Van Dishoeck et al., in prep.).

Data were simultaneously taken with the acousto-optical wide band spectrometer (WBS) and the correlator-based high-resolution spectrometer (HRS), in both horizontal and vertical polarizations. This paper focuses on data from the WBS, which covers 1140 MHz bandwidth at 1.1 MHz spectral resolution (~0.3 km s^{-1}) (Roelfsema et al. 2010). System temperatures range between 350 K around 1113 GHz and 450 K around 988 GHz; receiver 4a in V polarization shows particularly high values. Integration times (ON+OFF) were 193 s for the 1113 GHz and the 1102 GHz lines and 206 s for the 988 GHz line for each source, and the rms noise levels reached are 40–50 mK (Table 1). Observations were reduced with the *Herschel* interactive processing environment[1] (HIPE) version 2.8. The intensity scale is converted to T_{mb} using main beam efficiencies of 0.74. The double-side band continuum level was divided by 2 to make its brightness directly comparable to that of the lines, which are measured in single sideband.

3. Results

Observed water lines for the four studied regions are shown in Fig. 1. The H_2O $1_{11}-0_{00}$ line shows an absorption at the systemic velocity (V_{LSR}) in all sources. In all cases except G31.41+0.31, outflow wings are detected close to the main absorption, with a maximal shift of 3 km s^{-1}. These wings are seen in emission, which indicates an origin in hot, low-density (10^3 cm^{-3}) gas (Poelman & van der Tak 2007). Absorption features are seen over a wide velocity range in G29.96-0.02, W33A, W43-MM1, and more weakly in G31.41+0.31. The absorptions at velocity offsets >4 km s^{-1} likely originate in cold foreground clouds on the line of sight to the source. In contrast, the absorption features at lower velocity offsets are plausibly related to cold clouds surrounding the dense cores (which other studies call the protostellar envelopes), which are all part of large-scale molecular clouds (see Fig. 2). Table 3 presents a Gaussian decomposition of the line profiles around V_{LSR}; Appendix A shows Gaussian iterative decompositions of the absorption profiles of the ground-state transition over the full velocity range, showing several velocity components thanks to the high resolution in velocity of the HIFI instrument. The absorptions at V_{LSR} are saturated for G31.41+0.31 and W33A and nearly saturated for the other sources, which indicates abundances around $\sim10^{-9}$ for the outer cold parts of the massive dense cores (Poelman & van der Tak 2007).

The H_2O $2_{02}-1_{11}$ line always appears in emission and shows a broad and a narrower velocity component (Fig. 1). In addition, the spectra of G31.41+0.31 and W43-MM1 show two well-defined self-absorption features that appear at the source velocity. With its high E_{up}, this transition mainly traces warm gas, and the presence of these absorption features in G31.41+0.31 and W43-MM1 suggests a higher water abundance in these sources than in G29.96–0.02 and W33A. The components seen in emission have Gaussian shapes, with one wider ($FWHM$ = 20–40 km s^{-1}) than the other ($FWHM$ = 6.4–8.0 km s^{-1}). We associate the broad component with high-velocity outflows associated with the protostar also seen in $1_{11}-0_{00}$ line emission. This component is symmetric with respect to the source velocity in G29.96–0.02 and W43-MM1, blueshifted by 2.8 km s^{-1} in W33A, and redshifted by 4.4 km s^{-1} in G31.41+0.31 (Table 3). The narrower (hereafter "medium") component is potentially associated with shocked surrounding material where water is released in the gas phase. Indeed, shocks occur at the interface between jets and the surrounding dense envelope, with a velocity close to that of the massive dense core. Similar results are found in Kristensen et al. (2010), Johnstone et al. (2010), and Chavarría et al. (2010).

The $H_2^{18}O$ $1_{11}-0_{00}$ transition is seen in absorption at the source velocity in G31.41 and W43-MM1, which is not saturated. This feature originates in the massive envelope. In G29.96, the pure emission profile of this transition implies a warm diffuse gas origin. Since G29.96 is also the brightest source in the narrower component of the 988 GHz line, we suggest that the $H_2^{18}O$ emission is dominated by shocks at the interface between jets and the envelope. The P-Cygni-like profile for W33A is a mix of both behaviors: the sum of an absorption feature due to the massive core and emission from an outflow. The emission is only seen in the red-shifted part of the profile is consistent with the outflow components seen in 1113 GHz and 988 GHz lines, which are also the most powerful on the red part of the spectrum.

4. Discussion and conclusions

To derive the water abundance in the four massive dense cores, we removed features related to outflows and foreground clouds from the spectrum before any line modeling. The high spectral resolution of HIFI is essential in this process, in particular for

[1] http://herschel.esac.esa.int/

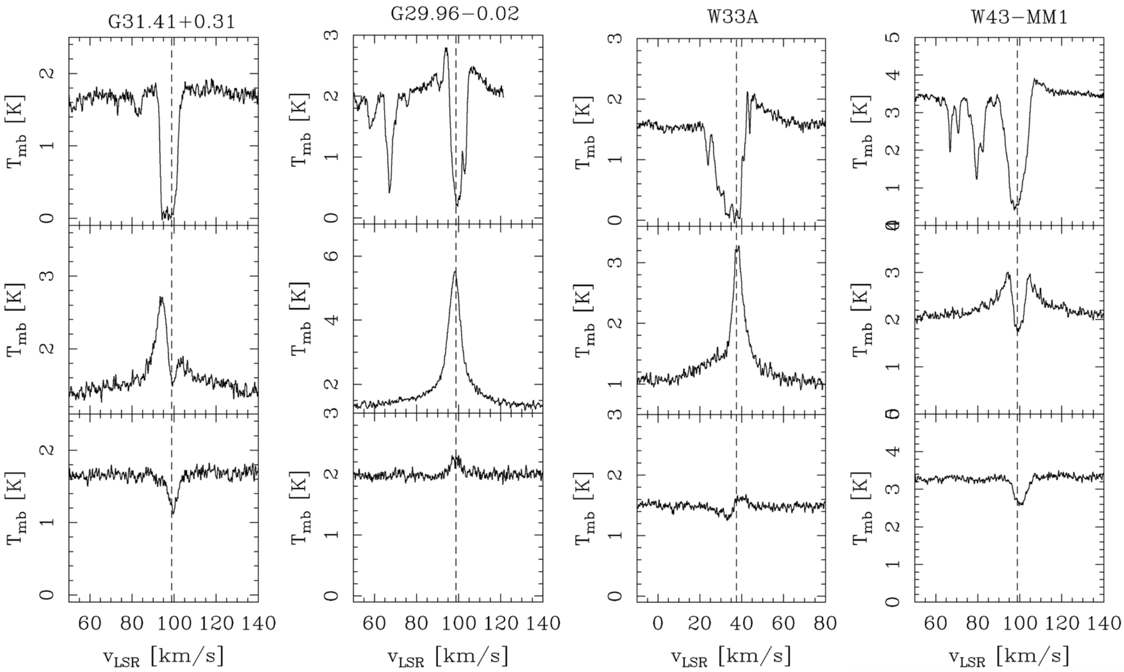

Fig. 1. *Herschel*/HIFI spectra of the H_2O 1_{11}–0_{00} (*top*), H_2O 2_{02}–1_{11} (*middle*) and $H_2^{18}O$ 1_{11}–0_{00} (*bottom*) lines. Dashed lines are drawn at V_{LSR}.

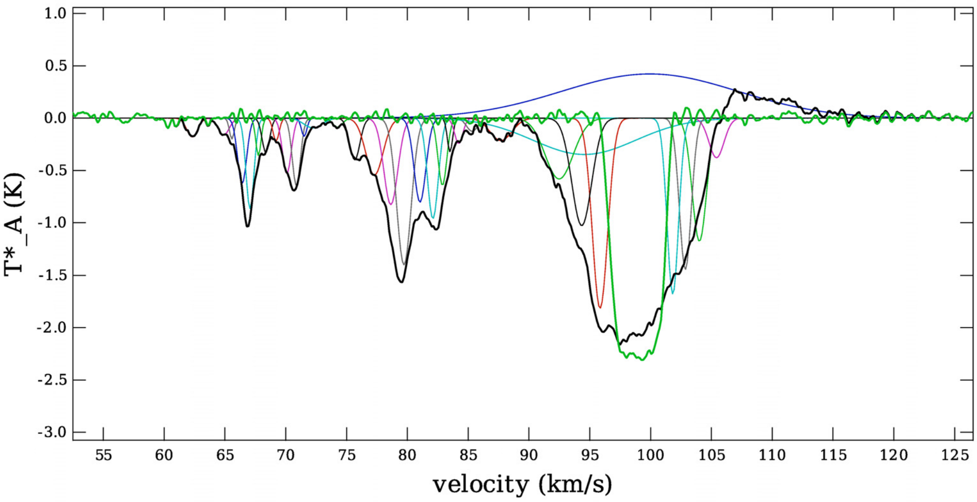

Fig. 2. Extraction of the saturated absorption of para-H_2O 1_{11}–0_{00} line in W43-MM1. Original profile appears in black bold, and the residual in green bold. Other colored lines show Gaussian components used to remove cold foreground clouds absorptions. The aim of the multiple colours is to better distinguish the components between themselves.

Table 3. Gaussian decomposition of the line profiles at velocities close to V_{LSR}.

Source	Para-H_2O (1_{11}–0_{00})			Para-H_2O (2_{02} – 1_{11})			Para-$H_2^{18}O$ (1_{11} – 0_{00})		
	V_{LSR} (km s^{-1})	T_{mb} (K)	ΔV (km s^{-1})	V_{LSR} (km s^{-1})	T_{mb} (K)	ΔV (km s^{-1})	V_{LSR} (km s^{-1})	T_{mb} (mK)	ΔV (km s^{-1})
G31.41+0.31	95.1	0.94*	3.7	94.6	1.37	6.4	99.5	0.27*	5.2
				99.3	0.42*	14.0			
				103.7	0.2	∼40			
G29.96-0.02	91.3	0.26*	3.9	97.8	1.10	21	98.5	290	6.0
	98.5	0.90	18.8	98.2	3.21	8.0			
	99.4	0.99*	8.4						
	103.2	0.40*	2.3						
W33A	35.9	0.85*	11.0	35.5	0.34	28	34.2	0.23*	11.8
	43.0	0.53	20.0	38.3	1.87	7.0	37.3	280	8.4
W43-MM1	98.7	0.87*	13.5	99.6	0.89	22	99.4	0.19*	8.7
	103.3	0.43	14.0	99.7	0.31*	6.8			

Notes. (*) Absorption lines are indicated in $T_{abs}/T_{continuum}$ scales.

Table 4. Model parameters and derived water abundances.

Source	M_{gas} ($M_\odot$)	r_{min} (AU)	r_{max} (AU)	$n(r_{min})$ (cm^{-3})	$n(r_{max})$ (cm^{-3})	$T(r_{min})$ (K)	$T(r_{max})$ (K)	X_{H_2O}	υ_{turb} (km s^{-1})
G31.41+0.31	1500	200	22 515	8.1×10^8	3.1×10^6	406	43.2	3.1×10^{-8}	1.4
G29.96-0.02	700	200	20 700	4.4×10^8	1.9×10^6	489	50.8	$<5.0 \times 10^{-10}$	1.1
W33A	4000	200	62 000	3.5×10^8	4.0×10^5	291	26.0	6.0×10^{-10}	1.6
W43-MM1	2000	200	27 500	5.0×10^8	2.3×10^6	243	24.7	4.0×10^{-8}	3.0
DR21[a]	1650	2000	60 520	1.6×10^7	1.5×10^5	117	23.3	2.0×10^{-10}	3.0
W3-IRS5[b]	250	200	12 000	2.9×10^8	2.7×10^6	480	54.7	2.0×10^{-8}	2.0

Notes. [(a)] Values from van der Tak et al. (2010) [(b)] Values from Chavarría et al. (2010).

the absorbers with velocities close to that of the central source. Studying the $H_2^{18}O$ $1_{11}-0_{00}$ transition prior to the others also facilitates disentangling the envelope contribution, since this line is not saturated because it has a lower optical depth than the main H_2O isotope.

Once the main contribution is extracted, we model its profile according to the method described in Marseille et al. (2008): first, the dust emission from the massive dense core is reproduced with the MC3D radiative transfer code (Wolf et al. 1999), including total luminosity and density profile from the literature (power-law index $p = -1.5$); second, the temperature profile obtained is used to model the line emission with the RATRAN code (Hogerheijde & van der Tak 2000). The free parameters are X_{H_2O}, the molecular abundance relative to H_2, and υ_{turb}, the turbulent velocity width.

Good fits are obtained for the $H_2^{18}O$ $1_{11}-0_{00}$ transition, which is not saturated, unlike the H_2O lines. The fitting considers both the line strength (area and width) and the profile shapes. We have computed a grid of X_{H_2O} and υ_{turb} values, adapting step by step the grid around the best χ^2. Using a $^{16}O/^{18}O$ ratio of 500, we proceed to model the main isotopic water lines. The H_2O abundance is kept constant in our models. We tried models with an abundance increase in the inner region where $T > 100$ K, but the current data do not favor those models above the constant-abundance models.

We estimate the absolute uncertainty in the retrieved H_2O abundance to be a factor of 10. Since we use the same modeling strategy as in the studies by van der Tak et al. (2010) and Chavarría et al. (2010), the abundances obtained should be comparable to better than a factor of 3. Our observed spread in abundances of a factor of ~100 is much greater than this uncertainty. The same range of abundances is found in other HIFI-based studies of high-mass star-forming regions (van der Tak et al. 2010; Chavarría et al. 2010), and also in previous work with ISO (Boonman et al. 2003) and from the ground (van der Tak et al. 2006).

In conclusion, for the massive-star forming regions described in this letter, we clearly detect the contribution of the envelope within the dense core. It is limited to a strong self-absorbed feature mainly seen in the ground-state line. To evaluate it, we first have to remove emission from outflow shocks and absorption by foreground clouds along the line of sight. The velocities of the absorbers indicate that some are part of the close environment of the source, while others are physically unrelated. The derived massive dense core abundances suggest a strong freeze-out of water on dust grains, and imply that water plays only a minor role in the thermal balance of the gas.

The H_2O line profiles do not seem to depend on the supposed evolutionary stage of the source. For example, the two "hot molecular cores" G31.41 and G29.96 show very different line profiles, and also their H_2O abundances differ by a factor of ~100. Also, the abundance variations that we have found do not seem related to the luminosity of the sources, their temperature or their turbulent velocity field. However, there are not enough cases treated for a statistical treatment. Future studies following the same procedure with more sources should resolve this issue. Within our sample, the highest H_2O abundances are derived for G31.41 and W43-MM1, which show self-absorbed $2_{02}-1_{11}$ line profiles (Fig. 1). As these sources are not the most luminous, hot, or active ones in our sample, the origin of such a high abundance is unclear.

Firm conclusions about a link between water emission behavior and the evolutionary stage of the source are limited by the small number of sources. Our data show that water is a useful tool for understanding the gas dynamics in and around massive star-forming regions. Future multiline studies of larger samples are highly promising for answering key questions about the formation of massive stars.

Acknowledgements. HIFI has been designed and built by a consortium of institutes and university departments from across Europe, Canada, and the United States under the leadership of SRON Netherlands Institute for Space Research, Groningen, The Netherlands, and with major contributions from Germany, France, and the US. Consortium members are: Canada: CSA, U.Waterloo; France: CESR, LAB, LERMA, IRAM; Germany: KOSMA, MPIfR, MPS; Ireland, NUI Maynooth; Italy: ASI, IFSI-INAF, Osservatorio Astrofisico di Arcetri- INAF; Netherlands: SRON, TUD; Poland: CAMK, CBK; Spain: Observatorio Astronómico Nacional (IGN), Centro de Astrobiología (CSIC-INTA). Sweden: Chalmers University of Technology – MC2, RSS & GARD; Onsala Space Observatory; Swedish National Space Board, Stockholm University – Stockholm Observatory; Switzerland: ETH Zurich, FHNW; USA: Caltech, JPL, NHSC.
HIPE is a joint development by the *Herschel* Science Ground Segment Consortium, consisting of ESA, the NASA *Herschel* Science Center, and the HIFI, PACS, and SPIRE consortia.

References

Boonman, A., Doty, S., van Dishoeck, E., et al. 2003, A&A, 406, 937
Chavarría, L., Herpin, F., Jacq, T., et al. 2010, A&A, 521, L37
Churchwell, E., Walmsley, C. M., & Cesaroni, R. 1990, A&As, 83, 119
de Graauw, Th., Helmich, F. P., Phillips, T. G., et al. 2010, A&A, 518, L6
Grosjean, A., Dubernet, M., & Ceccarelli, C. 2003, A&A, 408, 1197
Hatchell, J., & van der Tak, F. F. S. 2003, A&A, 409, 589
Hogerheijde, M. R., & van der Tak, F. F. S. 2000, A&A, 362, 697
Johnstone, D., Fish, M., M^cCoey, C., et al. 2010, A&A, 521, L41
Kristensen, L. E., Visser, R., van Dishoeck, E. F., et al. 2010, A&A, 521, L30
Marseille, M., Bontemps, S., Herpin, F., & et al. 2008, A&A, 488, 579
Motte, F., Schilke, P., & Lis, D. C. 2003, ApJ, 582, 277
Pilbratt, G. L., Riedinger, J. R., Passvogel, T., et al. 2010, A&A, 518, L1
Poelman, D. R., & van der Tak, F. F. S. 2007, A&A, 475, 949
Roelfsema, P. R., Helmich, F. P., Teyssier, D., et al. 2010, A&A, submitted
Sridharan, T. K., Beuther, H., Saito, M., Wyrowski, F., & Schilke, P. 2005, ApJ, 634, L57
van der Tak, F., van Dishoeck, E., Evans, I. N., & Blake, G. 2000, ApJ, 537, 283
van der Tak, F., Walmsley, C., Herpin, F., et al. 2006, A&A, 447, 1011
van der Tak, F., Marseille, M., Herpin, F., et al. 2010, A&A, 518, L107
Wolf, S., Henning, T., & Stecklum, B. 1999, A&A, 349, 839
Zinnecker, H., & Yorke, H. W. 2007, ARA&A, 45, 481

[1] Leiden Observatory, Leiden University, PO Box 9513, 2300 RA Leiden, The Netherlands
[2] Max Planck Institut für Extraterrestrische Physik, Giessenbachstrasse 1, 85748 Garching, Germany
[3] Institute of Astronomy, ETH Zurich, 8093 Zurich, Switzerland
[4] School of Physics and Astronomy, University of Leeds, Leeds LS2 9JT, UK
[5] INAF - Osservatorio Astrofisico di Arcetri, Largo E. Fermi 5, 50125 Firenze, Italy
[6] Université de Bordeaux, Laboratoire d'Astrophysique de Bordeaux, France; CNRS/INSU, UMR 5804, Floirac, France
[7] National Research Council Canada, Herzberg Institute of Astrophysics, 5071 West Saanich Road, Victoria, BC V9E 2E7, Canada
[8] Department of Physics and Astronomy, University of Victoria, Victoria, BC V8P 1A1, Canada
[9] Department of Radio and Space Science, Chalmers University of Technology, Onsala Space Observatory, 439 92 Onsala, Sweden
[10] SRON Netherlands Institute for Space Research, PO Box 800, 9700 AV, Groningen, The Netherlands
e-mail: `M.Marseille@sron.nl`
[11] Kapteyn Astronomical Institute, University of Groningen, PO Box 800, 9700 AV, Groningen, The Netherlands
[12] Observatorio Astronómico Nacional (IGN), Calle Alfonso XII,3. 28014 Madrid, Spain
[13] INAF - Istituto di Fisica dello Spazio Interplanetario, Area di Ricerca di Tor Vergata, via Fosso del Cavaliere 100, 00133 Roma, Italy
[14] Department of Astronomy, The University of Michigan, 500 Church Street, Ann Arbor, MI 48109-1042, USA
[15] California Institute of Technology, Division of Geological and Planetary Sciences, MS 150-21, Pasadena, CA 91125, USA
[16] Centro de Astrobiología. Departamento de Astrofísica. CSIC-INTA. Carretera de Ajalvir, Km 4, Torrejón de Ardoz. 28850, Madrid, Spain
[17] Astronomical Institute Anton Pannekoek, University of Amsterdam, Kruislaan 403, 1098 SJ Amsterdam, The Netherlands
[18] Department of Astrophysics/IMAPP, Radboud University Nijmegen, PO Box 9010, 6500 GL Nijmegen, The Netherlands
[19] Department of Physics and Astronomy, Denison University, Granville, OH 43023, USA
[20] LERMA and UMR 8112 du CNRS, Observatoire de Paris, 61 Av. de l'Observatoire, 75014 Paris, France
[21] University of Waterloo, Department of Physics and Astronomy, Waterloo, Ontario, Canada
[22] Observatorio Astronómico Nacional, Apartado 112, 28803 Alcalá de Henares, Spain
[23] INAF - Osservatorio Astronomico di Roma, 00040 Monte Porzio catone, Italy
[24] Centre for Star and Planet Formation, Natural History Museum of Denmark, University of Copenhagen, Øster Voldgade 5-7, 1350 Copenhagen K., Denmark
[25] Department of Astronomy, Stockholm University, Albania, 106 91 Stockholm, Sweden
[26] California Institute of Technology, Cahill Center for Astronomy and Astrophysics, MS 301-17, Pasadena, CA 91125, USA
[27] The University of Western Ontario, Department of Physics and Astronomy, London, Ontario, N6A 3K7, Canada
[28] Harvard-Smithsonian Center for Astrophysics, 60 Garden Street, MS 42, Cambridge, MA 02138, USA
[29] Department of Physics and Astronomy, Johns Hopkins University, 3400 North Charles Street, Baltimore, MD 21218, USA
[30] Max-Planck-Institut für Radioastronomie, Auf dem Hügel 69, 53121 Bonn, Germany
[31] Jet Propulsion Laboratory, 4800 Oak Grove Drive, MC 302-306, Pasadena, CA 91109 USA
[32] Department of Physics and Astronomy, University of Calgary, Calgary, T2N 1N4, AB, Canada
[33] Instituto de Radioastronomía Milimétrica (IRAM), Avenida Divina Pastora 7, Núcleo Central, 18012 Granada, Spain
[34] KOSMA, I. Physik. Institut, Universität zu Köln, Zülpicher Str. 77, 50937 Köln, Germany
[35] Microwave Laboratory, ETH Zurich, 8092 Zurich, Switzerland
[36] Centre d'Étude Spatiale des Rayonnements, Université de Toulouse [UPS], 31062 Toulouse Cedex 9, France
[37] CNRS/INSU, UMR 5187, 9 avenue du Colonel Roche, 31028 Toulouse Cedex 4, France

Appendix A: Massive dense core component extraction

The velocity profiles of the H_2O 1_{11}–0_{00} line show absorption features at several velocities. These absorption features arise in foreground clouds along the line of sight or in cold clouds in the neighborhood of the massive dense core, and are not saturated unlike the absorption from the massive envelope. In addition to these absorptions, some sources show H_2O emission from protostellar outflows.

This appendix presents our procedure for removing these features in order to extract the contribution from the envelope to the line profile. In contrast to others, absorption from this part of the object is saturated. We are then able to remove other features by iterative Gaussian fits. This process is helped by the high resolution in velocity provided by the *Herschel*/HIFI instrument, showing accurate and "bumpy" profiles in absorptions. Assuming that each bump corresponds to a velocity component, they are removed using the Gaussian fitting tool available in the HIPE software. Starting from the component with the lowest velocity, they are extracted one by one, using the residual of the previous removal to fit the next one. This way of fitting insures a very good extraction of velocity component, giving a quasi-unique final decomposition of the absorption features. Results of this process are given in Figs. 2, A.1, A.2, A.3 and Tables A.1, A.2, A.3, and A.4.

Table A.1. Gaussian fit parameters for the full extraction of the saturated absorptions of para-H_2O $1_{11}-0_{00}$ line in W43-MM1.

Component #	T_A^* (K)	$FHWM$ (km s^{-1})	$\upsilon_{\rm lsr}$ (km s^{-1})
1	–0.18	1.46	62.31
2	–0.16	1.50	64.90
3	–0.20	0.66	65.57
4	–0.63	1.22	66.41
5	–0.87	1.09	67.06
6	–0.36	0.71	67.75
7	–0.33	1.02	68.37
8	–0.22	0.82	69.20
9	–0.53	1.19	70.09
10	–0.65	1.10	70.87
11	–0.17	0.74	71.51
12	–0.09	2.46	72.25
13	–0.09	1.31	74.27
14	–0.40	1.40	75.67
15	–0.54	2.35	77.29
16	–0.83	1.89	78.64
17	–1.40	1.95	79.72
18	–0.80	1.59	81.04
19	–0.96	1.46	82.10
20	–0.64	1.19	82.89
21	–0.32	0.71	83.51
22	–0.21	2.95	87.69
23	–0.24	1.11	84.23
24	–0.13	1.52	85.33
25	0.42	23.94	99.94
26	–0.35	13.95	94.55
27	–0.58	3.78	92.48
28	–1.03	2.68	94.34
29	–1.82	2.08	95.84
30	–0.38	2.03	105.42
31	–1.18	1.95	104.01
32	–1.45	1.60	102.86
33	–1.68	1.55	101.83

Table A.2. Gaussian fit parameters for for the full extraction of the saturated absorptions of para-H_2O 1_{11}–0_{00} line in W33A.

Component #	T_A^* (K)	$FHWM$ (km s^{-1})	$\upsilon_{\rm lsr}$ (km s^{-1})
1	0.32	32.95	42.00
2	–0.48	2.92	23.87
3	–0.79	4.70	28.41
4	–0.80	3.64	31.06
5	–0.74	1.60	32.40
6	–1.12	1.75	33.52
7	–0.98	1.31	34.46
8	–0.41	1.00	43.83
9	–0.70	2.20	41.13
10	–1.24	1.91	39.40

Table A.3. Gaussian fit parameters for for the full extraction of the saturated absorptions of para-H_2O $1_{11}-0_{00}$ line in G29.96.

Component #	T_A^* (K)	$FHWM$ (km s^{-1})	$\upsilon_{\rm lsr}$ (km s^{-1})
1	–0.44	2.32	4.41
2	–1.12	2.30	6.01
3	–0.95	1.71	7.15
4	–0.89	1.30	8.08
5	–0.95	1.32	8.93
6	–0.38	1.04	9.91
7	–0.37	1.14	10.84
8	–0.43	1.06	11.68
9	–0.23	1.21	12.42
10	–0.11	4.55	16.85
11	–0.07	6.52	52.89
12	–0.31	1.13	57.62
13	–0.34	1.29	58.57
14	–0.25	3.12	60.10
15	–0.48	1.39	65.37
16	–1.03	2.00	66.76
17	–0.40	2.93	69.38
18	0.50	26.36	98.50
19	–0.24	3.17	91.42
20	–1.44	3.06	102.91

Table A.4. Gaussian fit parameters for for the full extraction of the saturated absorptions of para-H_2O 1_{11}–0_{00} line in G31.41.

Component #	T_A^* (K)	$FHWM$ (km s^{-1})	$\upsilon_{\rm lsr}$ (km s^{-1})
1	–0.08	1.36	3.79
2	–0.43	1.35	5.44
3	–0.99	1.06	6.44
4	–0.61	0.86	7.06
5	–0.35	0.68	7.57
6	–0.34	0.84	8.15
7	–0.19	0.88	8.89
8	–0.36	1.61	10.99
9	–0.59	1.31	11.72
10	–1.19	1.40	12.75
11	–0.49	0.98	13.53
12	–0.15	4.63	52.14
13	–0.21	4.53	82.84
14	0.06	10.92	119.53
15	0.10	25.85	99.02
16	–0.23	3.41	102.70

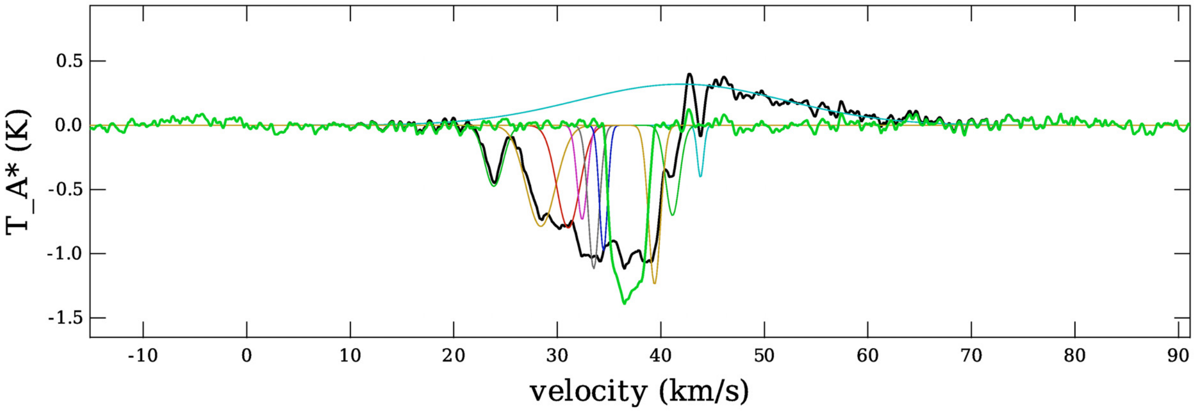

Fig. A.1. Extraction of the saturated absorption of para-H_2O $1_{11}-0_{00}$ line in W33A. Original profile appears in black bold, residual in green bold.

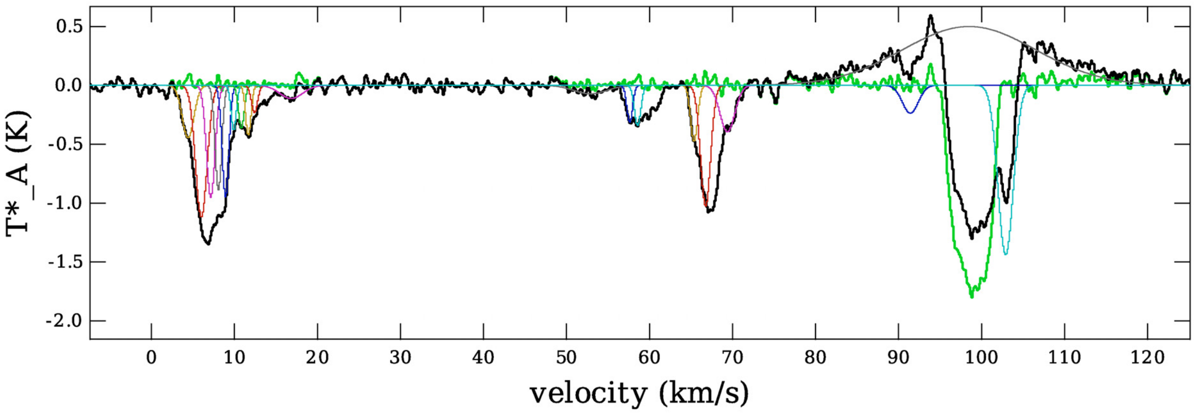

Fig. A.2. Extraction of the saturated absorption of para-H_2O $1_{11}-0_{00}$ line in G29.96. Original profile appears in black bold, residual in green bold.

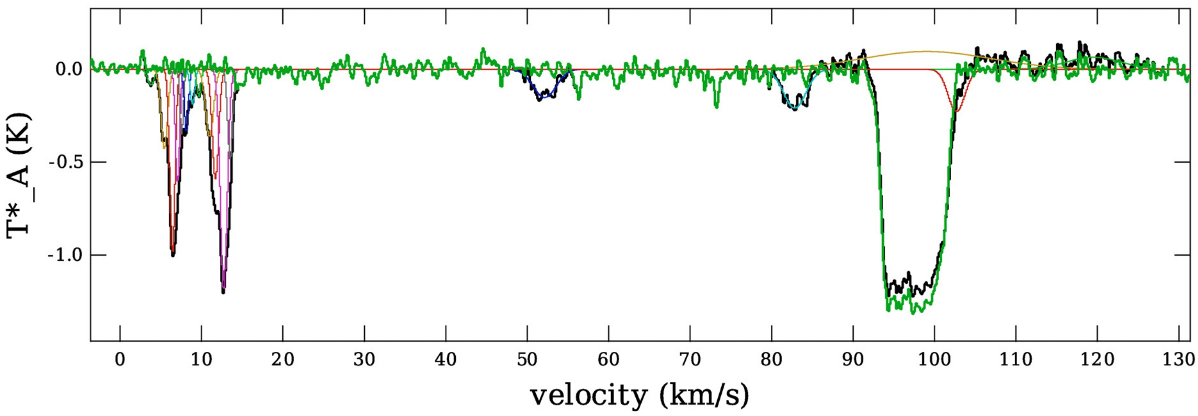

Fig. A.3. Extraction of the saturated absorption of para-H_2O $1_{11}-0_{00}$ line in G31.41. Original profile appears in black bold, residual in green bold.